Engineering Fracture Mechanics 276 (2022) 108879

Contents lists available at ScienceDirect

Engineering Fracture Mechanics

journal homepage: www.elsevier.com/locate/engfracmech

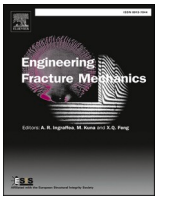

Analysis of displacement path dependence in mixed mode cohesive law

A. Arrese [a,*], F. Mujika [a], J. Renart [b,c], C. Sarrado [b,d]

[a] Mechanics of Materials, Faculty of Engineering of Gipuzkoa (UPV/EHU), San Sebastián, Spain
[b] AMADE, Polytechnic School (II), University of Girona, Carrer Universitat de Girona, 4, E-17003 Girona, Spain
[c] Serra Húnter Fellow, Generalitat de Catalunya, Spain
[d] AMTEC Composites, carrer Pic de Peguera 15, 17003 Girona, Spain

ARTICLE INFO

Keywords:
Mixed-mode I/II
Cohesive zone model
Cohesive law
Path dependence

ABSTRACT

In the present work, a general theoretical analysis is presented and novel mathematical expressions are derived to obtain the cohesive law of adhesive joints under mixed-mode loading.

It is theoretically stated that the mixed-mode truss-like cohesive laws, where the stress vector is forced to be parallel to the displacement vector, cannot adequately describe the fracture process when the displacement path is non-linear.

Finally, an experimental proof is given to show that in a Mixed Mode Bending test the difference between the phase angles of the stress vector and displacement differential vector must be taken into account when the displacement path becomes nonlinear, so that the cohesive stress will no longer be a function only of the magnitude of the displacement.

1. Introduction

In layered structures as adhesive joints, composite or sandwich structures, mixed mode fracture is often observed along interfaces due to anisotropy of the material or the loading conditions.

The cohesive zone model (CZM) is an effective tool to describe the delamination and debonding in layered structures.

Firstly introduced by Dugdale [1] and Barenblatt [2], in the CZM the fracture is modeled as a gradual phenomenon that relies on a traction separation law, assumed as the constitutive law of the material, which describes the failure behavior of the material [3]. The extension of the damaged zone is called the fracture process zone (FPZ).

Since Needleman [4] incorporated a mode I CZM in a continuum mechanics numerical model, the use of cohesive laws has been widely spread in finite element models to simulate the failure of layered materials and structures [5,6,7,8] and has been generalized to account for mixed mode fracture [9,10,11,12,13,14].

When accounting for mixed mode fracture, the fracture process zone is subjected to normal and tangential relative displacements. Thus, the general idea is that the law that describes the fracture process relates the cohesive stress vectors across the crack surfaces to the relative displacement vectors between those surfaces [15].

The mixed mode cohesive laws can be classified in different ways [16], for instance: **Coupled/Uncoupled** cohesive laws depending on whether the normal and shear stresses depend only on their corresponding displacement or not, respectively, or; **path-independent/path- dependent** depending on whether they can be derived from a potential function or not.

* Corresponding author.
E-mail address: ainhoa.arrese@ehu.eus (A. Arrese).

https://doi.org/10.1016/j.engfracmech.2022.108879
Received 19 May 2022; Received in revised form 21 September 2022; Accepted 10 October 2022
Available online 19 October 2022

Nomenclature

Acronyms

CZM	The cohesive zone model
MMB	Mixed-mode bending test
FPZ	Fracture Process Zone
DIC	Digital Image Correlation
ECL	Equivalent Crack Length approach

Latin alphabet

B	Mixed mode ratio
b	specimen width
c	loading lever length
D	damage variable
E_{11}, E_{22}, E_{33}	longitudinal, in-plane and out-of-plane elastic moduli, respectively
G_{12}	in-plane shear modulus
G_{13}, G_{23}	out-of-plane shear moduli
g	glue line
$2h$	total thickness of the specimen.
J	fracture resistance (work of cohesive stresses)
J_c	fracture energy
J_I	mode I part of the work of cohesive stresses
J_{II}	mode II part of the work of cohesive stresses
K	penalty stiffness of bi-linear cohesive law
L	half-span of specimen
P	applied load at the lever arm
T	Stress vector perpendicular to the integration path Γ
w	Strain energy density
u	Displacement vector.

Greek alphabet

Γ	Integration path
Δ_n	Opening displacement at the crack tip
Δ_{n0}	Opening displacement for damage initiation
Δ_{nf}	Opening displacement for complete failure
Δ_t	Shear-displacement at the crack tip
Δ_{t_F}	Shear displacement at the crack tip associated with the onset of frictional effects
Δ_{t0}	Shear-displacement for damage initiation
Δ_{tf}	Shear-displacement for complete failure
θ	phase angle of the cohesive stresses vector
Θ	rotation angle at A, B, C and D; positive in counterclockwise direction
λ	Displacement at the crack tip
λ_{lin}	Limit of the linear region of displacement path at the crack tip
λ_F	Displacement at the crack tip associated with the onset of frictional effects
μ	Cohesive stress
σ	Cohesive normal stress
σ_0	Peak of the cohesive normal stress
τ	Cohesive shear stress
τ_0	Peak of the cohesive shear stress
φ	Phase angle of the displacement differential vector
ψ	Phase angle of the displacement vector

For path-independent mixed-mode cohesive laws, the work of the cohesive tractions depends only on the normal and tangential separations and not on the history of the relative displacements between surfaces.

Recently, Goutianos [17] has provided experimental evidences confirming that considering path independence in unidirectional composites with large-scale fracture process zones is a reasonable assumption.

Concerning the experimental determination of the cohesive law in mixed mode, Sørensen et al, [18,19,20] developed the method originally proposed by Suo et al. [21] to determine the cohesive laws and extended it to mixed mode I/II [22,23]. The data analysis involves a fitting procedure to determine an approximate potential function so that the cohesive stresses can be determined by partial differentiation.

Sarrado et al. [24] applied the direct method to analyze experimentally the effect of the bond configurations on the cohesive laws in both pure modes I and II and mixed mode I/II. The cohesive laws were computed assuming that the resulting mixed mode cohesive stress is solely a function of the magnitude of the total displacement at the crack tip.

Recently, Oliveira et al. [25] presented a study that addresses the experimental identification of the mixed mode cohesive law of *Pinus Pinaster*. Assuming the linearity of the displacement path during the mixed mode test and the existence of a potential function, the mixed mode cohesive law is directly computed.

The objective of the present work is to develop a new general approach to experimentally obtain the cohesive law of an adhesive layer under mixed-mode loading. The method is based on the *J*-Integral and it does not require an initial assumption of path linearity or data-fitting procedure.

The paper is organized as follows; in **Section 2,** the theoretical background is presented and the mathematical expression to obtain the mixed mode cohesive law is elicited. In **Section 3,** the specific case of truss-like cohesive laws is analyzed and the conditions that must fulfill are defined. In **Section 4,** the experimental Mixed Mode Bending Test (MMB) and the data reduction method applied are presented to study the cohesive law for mixed mode I/II fracture of different bond configurations. In **Section 5,** results of the measured displacement path, the evaluated J integral and the determined cohesive law are presented and the effects of the path non linearity and its source are discussed. Finally, concluding remarks are presented in **Section 6.**

2. J Integral and the cohesive law

The path independent *J*-integral, developed by Rice [26] can be used to calculate the fracture resistance *J* during the crack growth.

$$J = \int_{\Gamma} \left[w dy - T \frac{\partial u}{\partial x} ds \right] \tag{1}$$

In which w is the strain energy density; T is the stress vector perpendicular to the integration path Γ; and u is the displacement vector.

By evaluating the path independent J integral locally around the cohesive zone, yields [22]:

$$J = \int_0^{\Delta_n} \sigma d\Delta_n + \int_0^{\Delta_t} \tau d\Delta_t \tag{2}$$

where σ, τ, Δ_n and Δ_t are the cohesive normal stress, shear stress, opening and shear displacement at the crack tip, respectively as shown in Fig. 1.

The result of the integral *J* Eq. (2) is the work per unit fracture area of the cohesive stresses. When the fracture process zone is fully developed, Δ_n and Δ_t reach critical values and the cohesive stresses are equal to 0, and the *J* is equal to the work of separation, J_c, called fracture energy.

If it is assumed that the cohesive stress components are derived from the potential function *J*, what implies that d*J* is an exact differential, from Eq. (2) it yields,

$$\vec{\nabla} J = \vec{\mu}(\Delta_n, \Delta_t) \quad \sigma = \left[\frac{\partial J}{\partial \Delta_n} \right]_{\Delta_t} \quad \tau = \left[\frac{\partial J}{\partial \Delta_t} \right]_{\Delta_n} \tag{3}$$

Eq. (3) implies that the work performed by the cohesive stresses is displacement path independent, i.e. it only depends on the current displacement and not on the displacement history.

Defining $\vec{\mu}$ as the cohesive stress vector and $\vec{\lambda}$ as the displacement vector at the crack tip

$$\vec{\mu} = \sigma \hat{i} + \tau \hat{j} \qquad \vec{\lambda} = \Delta_n \hat{i} + \Delta_t \hat{j} \tag{4}$$

Eq. (2) can be written as the following dot product [27]:

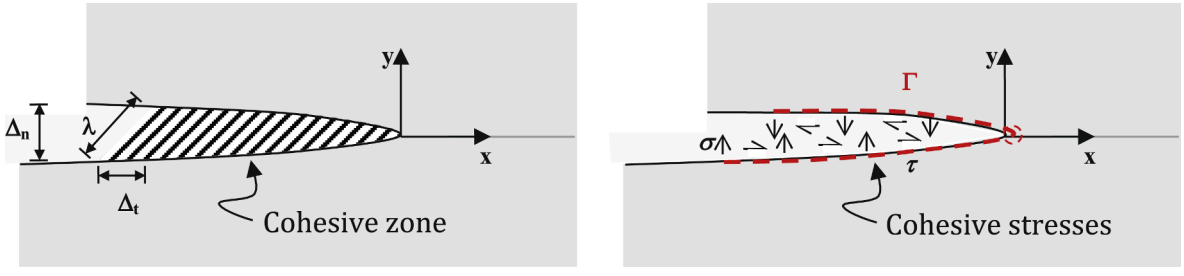

Fig. 1. Fracture process zone under mixed mode crack tip displacement. A) Definition of normal, tangential and total crack tip displacement. B) Integration path for the J integral.

$$J = \int_0^{\lambda} \vec{\mu} \cdot d\vec{\lambda} = \int_0^{\lambda} \mu \, d\lambda \, \cos(\theta - \varphi) \tag{5}$$

where θ is the phase angle of the cohesive stresses vector and φ is the phase angle of the displacement differential vector as shown in Fig. 2, defined as:

$$\theta = arctan\left(\frac{\tau}{\sigma}\right) \qquad \varphi = arctan\left(\frac{d\Delta_t}{d\Delta_n}\right) \tag{6}$$

According to Eq. (5), the cohesive stress can be determined as:

$$\mu(\lambda, \theta, \varphi) = \frac{dJ}{d\lambda} \frac{1}{cos(\theta - \varphi)} \tag{7}$$

According to Eq. (7), it can be concluded that for the magnitude of the cohesive stress, μ, to be a uniquely a function of the magnitude of the displacement, λ, the cohesive stress vector and the differential displacement vector should be parallel i. e. $\theta = \varphi$.

In general, assuming that $\theta \neq \varphi$, it is necessary to evaluate both phase angles in order to obtain the cohesive stresses, as depicted in Fig. 3.

The displacement fields at the crack tip can be measured [24] or obtained based on a specific data reduction method [29,36–38], so the $\varphi = arctan\left(\frac{d\Delta_t}{d\Delta_n}\right)$ is assumed to be known.

It should be noted that as shown in Fig. 3, the phase angle of the displacement vector (ψ) and the phase angle of the differential displacement vector (φ) are different in general terms.

On the other hand, since we do not know the explicit function of J as a function of Δ_n and Δ_t, i.e. the surface $J(\Delta_n, \Delta_t)$ is unknown, we cannot perform the partial derivatives in Eq. (3) to obtain the stress components and consequently the phase angle θ. Being mode I and mode II independent fracture modes [28,29], the normal and shear components of the cohesive stress can be obtained from $dJ = dJ_I + dJ_{II} = \sigma d\Delta_n + \tau d\Delta_t$ as:

$$\sigma = \frac{dJ_I}{d\Delta_n} \quad \tau = \frac{dJ_{II}}{d\Delta_t} \tag{8}$$

Being B the global mixed mode ratio defined as $B = \frac{J_{II}}{J}$, the following relation can be obtained

$$\frac{dJ_{II}}{dJ_I} = \frac{\tau}{\sigma}\frac{d\Delta_t}{d\Delta_n} = \frac{BdJ + JdB}{(1-B)dJ - JdB} = tan\theta tan\varphi \tag{9}$$

The relation between the phase angle of the cohesive stress vector and the phase angle of the displacement differential vector with the mixed mode ratio evolution shown in Eq. (9) must be satisfied at any point within the cohesive zone.

If the global mixed mode ratio remains constant during the test, Eq. (9) becomes in:

$$\frac{dJ_{II}}{dJ_I} = \frac{\tau}{\sigma}\frac{d\Delta_t}{d\Delta_n} = \frac{B}{(1-B)} \tag{10}$$

Therefore, according to Eq. (6) and Eq. (10), the phase angle of the cohesive stresses can be derived as:

$$\theta = arctan\left(\frac{\tau}{\sigma}\right) = arctan\left(\frac{B}{(1-B)}\frac{d\Delta_n}{d\Delta_t}\right) \tag{11}$$

Thus the normal and shear components of the cohesive stress vector, Eq. (7), can be derived in terms of displacement path as:

$$\sigma = \frac{dJ}{d\lambda}\frac{\cos(\theta)}{cos(\theta - \varphi)} \quad \tau = \frac{dJ}{d\lambda}\frac{\sin(\theta)}{cos(\theta - \varphi)} \tag{12}$$

From the above Eq (10), it follows that, if global mixed mode ratio remains constant, the variation of the phase angles θ and φ are inversely proportional. Therefore, even if the stress vector and displacement vector are not parallel, a linear displacement field $\varphi =$

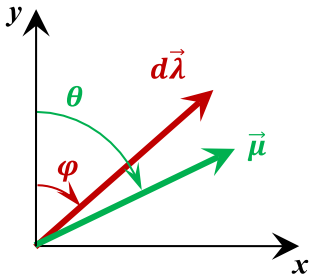

Fig. 2. Schematic definition θ and φ, where y is the opening direction and x the shear direction, see Fig. 1.

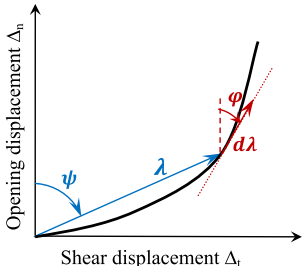

Fig. 3. Schematic definition ψ and φ.

ψwill be the one that provides the minimum difference in phase angles and consequently, the cosine value closest to one. The analysis is valid for coupled and uncoupled cohesvie laws, as Eq. (8) is valid for both cases.

3. Truss-like cohesive law

The truss-like mixed mode cohesive laws are constructed using energy based interpolation between pure modes I and II according to two interaction criteria: one for the initiation of the failure and another for the complete failure.

According to Goutianos et al [16] for bilinear truss like mixed mode cohesive laws (Fig. 4) that are derived from a potential function, the cohesive stress, μ, must be only a function of the magnitude of the displacement, λ

$$\mu(\lambda) = \frac{dJ}{d\lambda} \tag{13}$$

If this assumption is fulfilled, then the phase angle of the cohesive stress vector,θ and the phase angle of the opening displacement vector $\psi = arctan\left(\frac{\Delta_t}{\Delta_n}\right)$ must be identical for any point within the cohesive zone, $\theta = \psi$. i.e., the stress vector must follow the crack tip displacement vector as:

$$\sigma = K(1-D)\Delta_n \qquad \tau = K(1-D)\Delta_t \tag{14}$$

where K is the penalty stiffness and D the damage variable.

Then, the condition that must be fulfilled for Eq. (7) and Eq. (13) to be equal is that the phase angle of the cohesive stress vector,θ, and the phase angle of the crack tip displacement differential vector φ must be identical:

$$\theta = \varphi \quad \Rightarrow \quad tan\theta = tan\varphi \quad \Rightarrow \quad \frac{\tau}{\sigma} = \frac{d\Delta_t}{d\Delta_n} \tag{15}$$

Combining Eq. (14) and Eq. (15) yields to

$$\frac{\tau}{\sigma} = \frac{\Delta_t}{\Delta_n} = \frac{d\Delta_t}{d\Delta_n} \tag{16}$$

According to Eq. (16), assuming that the evolution of the fracture energy is only dependent on the magnitude of the displacement, i.e.$\cos(\theta-\varphi) = 1$, implies the linearity of the displacement path.

Being B the global mixed mode ratio, replacing the condition of Eq. (16) in Eq. (9) yields:

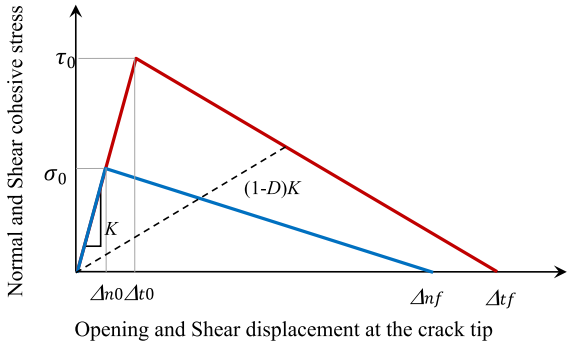

Fig. 4. Schematic illustration of truss-like bi-linear cohesive laws (normal and tangential directions).

$$\frac{dJ_{II}}{dJ_I} = \left(\frac{d\Delta_t}{d\Delta_n}\right)^2 = \left(\frac{\tau}{\sigma}\right)^2 = \left(\frac{\Delta_t}{\Delta_n}\right)^2 = \frac{BdJ + JdB}{(1-B)dJ - JdB} \tag{17}$$

If the global mixed mode ratio remains constant, Eq. (17) is reduced to:

$$\frac{\tau}{\sigma} = \frac{\Delta_t}{\Delta_n} = \frac{d\Delta_t}{d\Delta_n} = \sqrt{\frac{B}{(1-B)}} \tag{18}$$

Being the components of the opening displacement vector:

$$\begin{aligned} \Delta_n &= \sqrt{(1-B)}\lambda \\ \Delta_t &= \sqrt{B}\lambda \end{aligned} \tag{19}$$

And the components of the cohesive stress vector:

$$\begin{aligned} \sigma &= \sqrt{(1-B)}\mu \\ \tau &= \sqrt{B}\mu \end{aligned} \tag{20}$$

In summary, Eq. (16) implies that for truss like cohesive laws, the cohesive stress magnitude can be derived from a potential function only when the displacement path is linear. Therefore, the subsequent equations will only be valid in the case of a linear displacement path.

From this we conclude, as did Goutianos et al. [16], that if the displacement path is not linear, to assume that the stress vector is parallel to the displacement vector is not correct; in other words, the truss-like cohesive laws do not allow to adequately describe the fracture process when the displacement path is not linear.

4. Experimental work

4.1. Material and specimen configuration

The specimens tested were secondary bonded joints made of T800S/M21 carbon/epoxy unidirectional prepreg glued by a FM-300 epoxy adhesive film. An initial 60 mm long artificial crack was created by inserting a Teflon insert at one of the ends.

All the specimens had the following dimensions: a nominal length of 250 mm and a nominal width $b = 25$ mm. Specimens with different adherend and adhesive thicknesses were tested as shown in Table 1. The elastic properties of the adherends are $E_{11} =$ 134.7GPa, $E_{22} = E_{33} = 7.7$GPa and $G_{12} = G_{13} = 4.2$GPa [24].

4.2. MMB fracture test

Mixed-mode bending test (MMB) depicted in Fig. 5, was performed to characterize the adhesive under mixed mode fracture.

The MMB tests were carried out based on the procedure described in the ASTM D6671M-13 test standard [30]. All the tests were carried out on a support with a span length of $2L_0 = 150$ mm, and an initial crack length of 40 mm was set to assess the full development of the FPZ before the damaged zone reached the loading point.

The MMB lever arm was set for each particular test depending on the specimen thickness and the aimed mixed-mode ratio.

The MMB tests were run under displacement control in a servohydraulic MTS 858 testing machine using a 5 kN load cell.

The displacement rate was varied from 0.5 mm/min to 2.0 mm/min in order to get a constant strain rate for each specimen thickness and to ensure quasi-static crack growth. The displacement refers to the crosshead displacement of the testing machine.

The specimens were painted with a random black on white speckle pattern in one edge to measure the displacement at the crack tip using a Digital Image Correlation (DIC) system with a theoretical spatial resolution of 0.06 μm for the tests performed.

Four NA3-30 capacitive dielectric liquid-based inclinometers from SEIKA Mikrosystemtechnik GmbH were installed at load introduction points (points A, B, C and D in Fig. 5). The measurement range of the inclinometers was of ± 30º, and a resolution below 0.005° [24].The rotations, crosshead displacements and load were continuously recorded while the FPZ was being developed [31].

Table 1
Specimen configurations being g the position of the Teflon insert [24], t is the adhesive thickness and 2 h the total specimen thickness.

Specimen	$2h$ (mm)	Layup	t (mm)
A1T1	3.12 ± 0.06	$[0]_8/g/[0]_8$	0.21 ± 0.02
A2T1	4.60 ± 0.08	$[0]_{12}/g/[0]_{12}$	0.21 ± 0.02
A2T2	4.80 ± 0.10	$[0]_{12}/g/[0]_{12}$	0.37 ± 0.01
A3T1	6.05 ± 0.23	$[0]_{16}/g/[0]_{16}$	0.21 ± 0.02

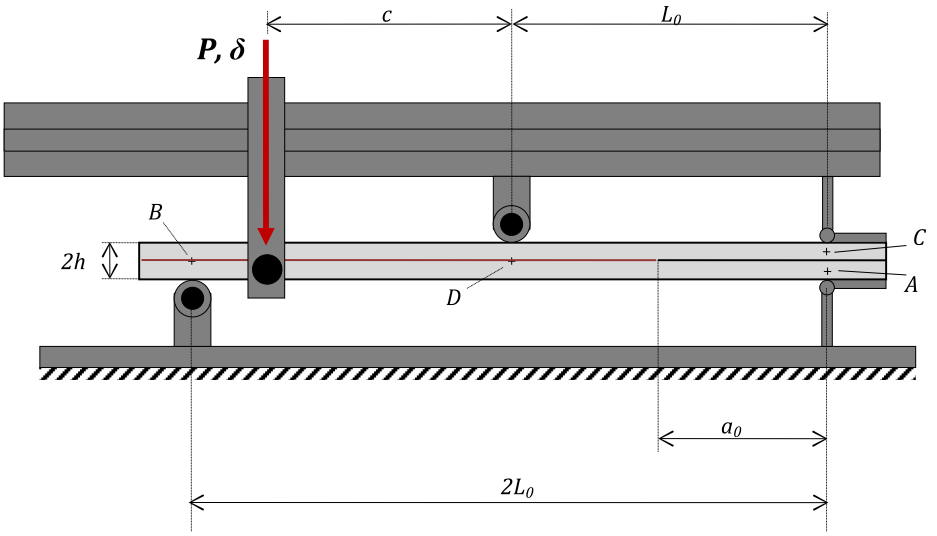

Fig. 5. Schematic of the MMB specimen.

4.3. Data reduction method

J, J_I and J_{II} are obtained according to the closed form solutions presented by Sarrado et al. [32] based on the measured rotations and the load:

$$J = \frac{P}{b}\left[\left(\frac{1}{2}-\frac{C}{2L}\right)\Theta_A + \left(\frac{1}{2}+\frac{C}{2L}\right)\Theta_B + \left(\frac{C}{L}\right)\Theta_C - \left(1+\frac{C}{L}\right)\Theta_D\right]$$

$$J_I = \frac{P}{2b}\left[\left(\frac{3C}{2L}-\frac{1}{2}\right)(\Theta_C - \Theta_A)\right]$$

$$J_{II} = \frac{P}{b}\left(\frac{1}{2}+\frac{C}{2L}\right)\left[\Theta_B - 2\Theta_D + \frac{1}{2}(\Theta_A + \Theta_C)\right] \quad (21)$$

Where b is the specimen width, c is the loading lever length, L is the half-span of specimen and $2h$ is the total thickness of the specimen. P is the absolute value of the applied load at the lever arm and Θ is the rotation angle at the points A, B, C and D as shown in

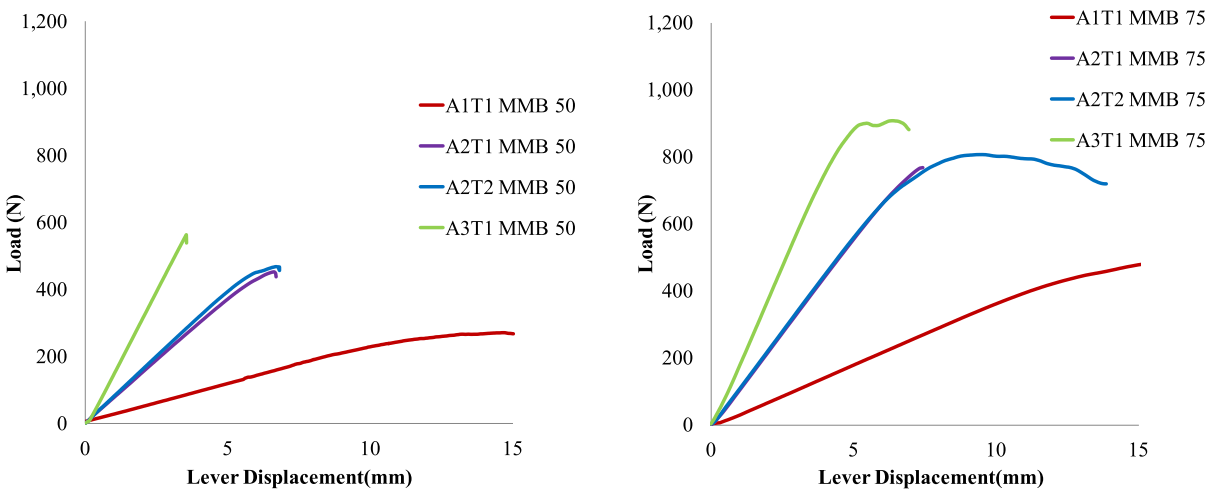

Fig. 6. Load Displacement curves a) MMB50% and b) MMB75%

Fig. 5, being positive the rotation in counterclockwise direction.

The crack tip displacement was monitored by DIC system at the initial crack tip position.

Finally, the cohesive stresses without neglecting the phase difference θ-φ were determined according to Eq. (7)

The cohesive stresses assuming truss-like behavior neglecting the phase difference θ-φ were determined according Eq. (13).

5. Results and discussion

Four different specimen configurations have been tested combining two adhesive thicknesses and three adherend thicknesses in two mixed mode ratios 50% and 75%.

The load displacement curves of 8 tests are presented in Fig. 6. As it can be seen, unstable crack propagation was obtained for A3T1 specimens from the MMB 50% test. It was not possible to obtain the complete cohesive law from these specimens, as the FPZ had not been fully generated when a sudden crack propagation occurred.

The J-λ curves shown in Fig. 7 have been computed as described in section 4.3, where the fracture energy is determined according to Eq (21), replacing the applied load at the lever arm and the measured rotation angles at A, B, C and D. The crack tip displacement λ is the Euclidean norm of the normal and shear displacements measured by DIC.

Regarding the crack tip displacement field, Fig. 8 shows the displacement path corresponding to MMB 50% on the left and MMB 75% on the right.

As depicted in Fig. 8, the displacement path is nonlinear for all the conducted mixed-mode tests. It is noticeable that fracture is shear dominant during the first stages of crack growth and progressively changes to normal as damage grows. A similar evolution of the displacement path has already been reported experimentally [33] and numerically [34,35].

Furthermore, Fig. 8 shows that the evolution of the crack tip displacement path is significantly dependent on the adherend thickness for the MMB 75% test, but not on the adhesive thickness (Fig. 8b). This dependence is practically nonexistent for the MMB 50% test (Fig. 8a).

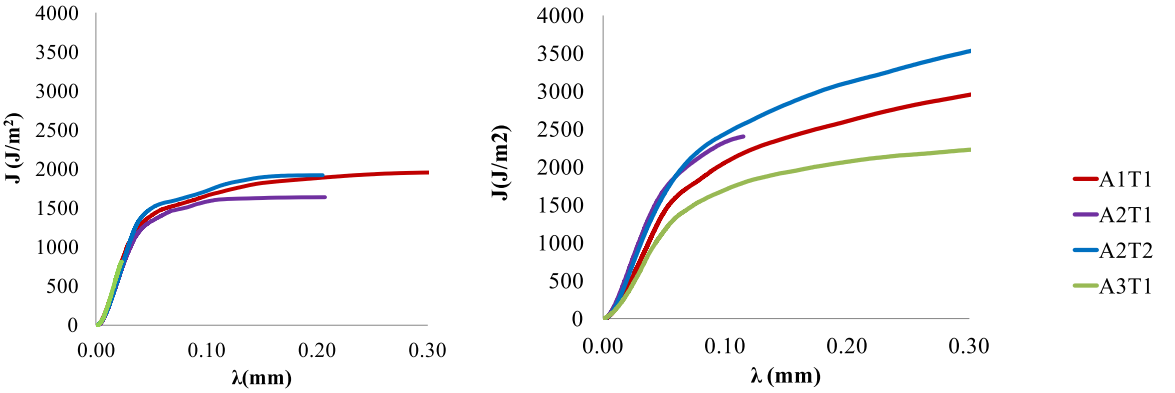

Fig. 7. J vs. crack tip displacements of (a) the MMB 50% tests conducted and (b) the MMB 75% tests conducted.

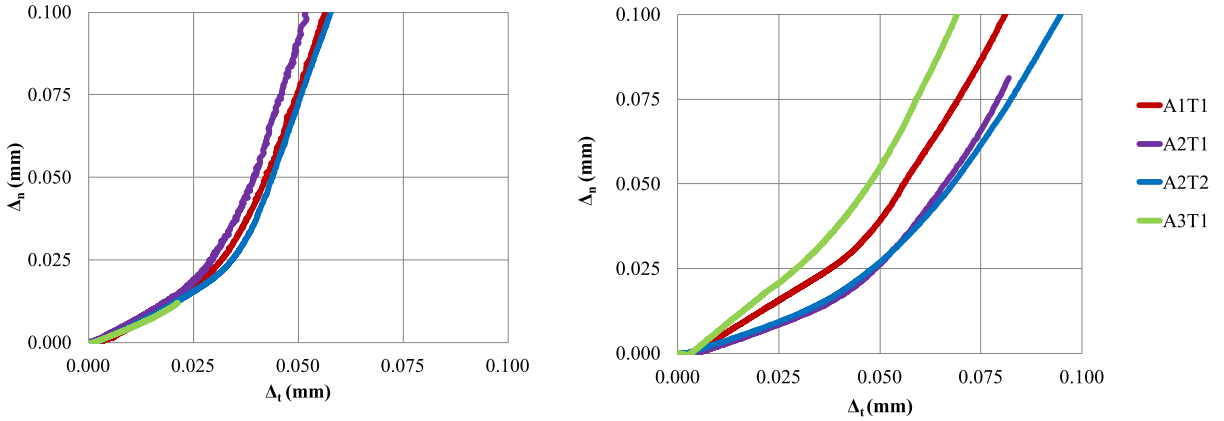

Fig. 8. Crack tip displacement path (a) the MMB 50% tests conducted and (b) the MMB 75% tests conducted.

Cohesive laws determined by Eq. (13) for MMB 50% and MMB 75% are shown in Fig. 9**a and 9b**, respectively.

According to Fig. 9, the effect of adhesive and adherend thickness on the fracture toughness is only noticeable for the MMB 75% test, as for the J(λ) curve depicted in Fig. 7**b**.

Both mixed mode ratios show a remaining cohesive stress for large crack tip displacement that may be indicative of friction at the fractured interface [24] or friction due to the FPZ being extended to the midpoint loading position of the MMB specimens as a result of the long FPZ inherent to the adhesive high toughness. The steady value of the cohesive stress is higher for MMB 75%.

In order to analyze the effect of displacement path nonlinearity on the cohesive law, Figs. 10 and 11, show the evolution of $Cos^{-1}(\theta\text{-}\varphi)$ corresponding to MMB 50% and MMB 75%, respectively, for all the tested configurations.

At a first glance, Figs. 10 and 11 show two regions clearly differentiated.

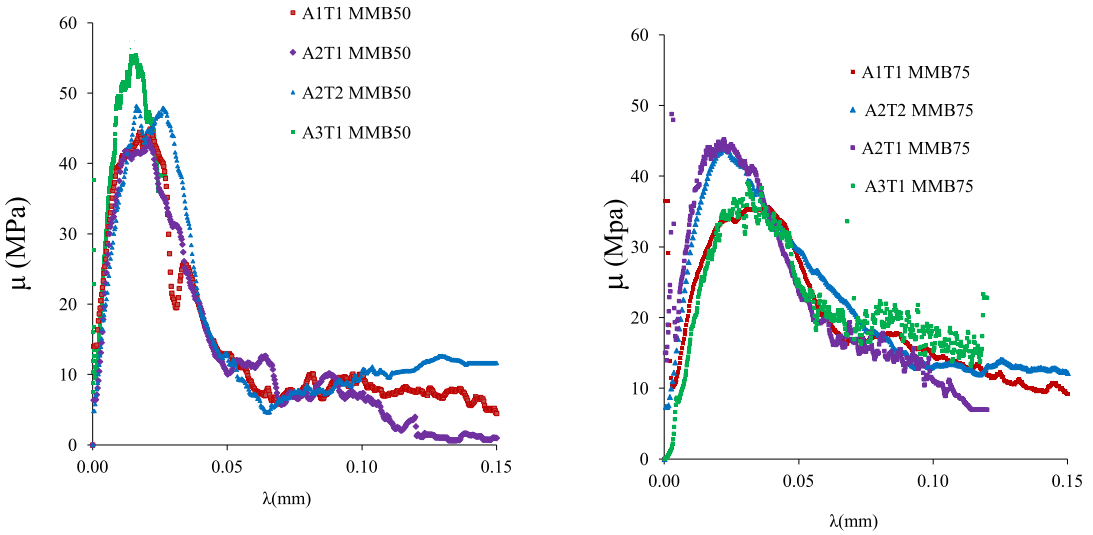

Fig. 9. Cohesive laws for applied mixed-mode ratio of a) 50% and b) 75%.

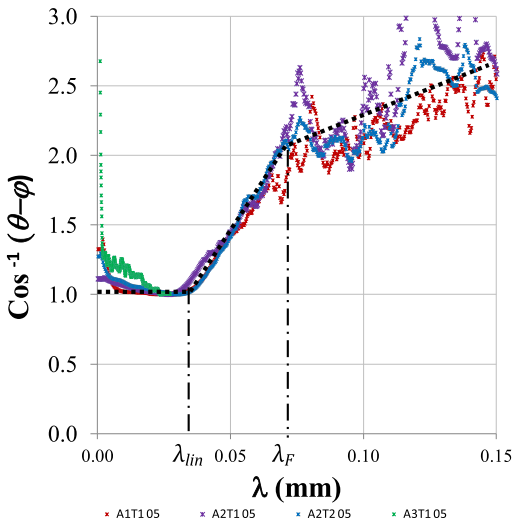

Fig. 10. Evolution of $Cos^{-1}(\theta\text{-}\varphi)$ for applied mixed-mode ratio of 50%, being the dashed lines the trend curves.

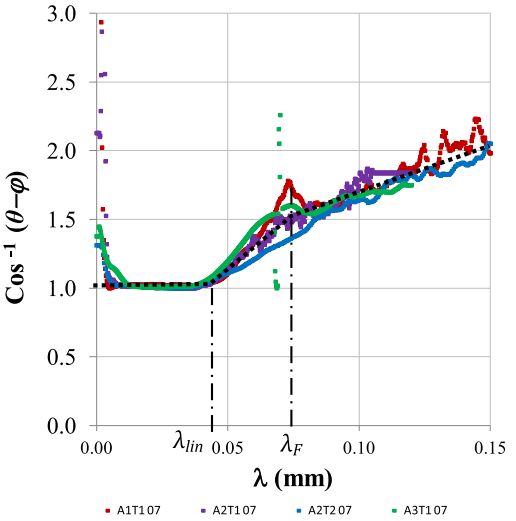

Fig. 11. Evolution of $Cos^{-1}(\theta\text{-}\varphi)$ for applied mixed-mode ratio of 75% being the dashed lines the trend curves.

- The first $0 < \lambda < \lambda_{lin}$, where $\theta \sim \varphi$ and $Cos^{-1}(\theta\text{-}\varphi) \cong 1$, corresponds to the linear part of the displacement path. This region arises at the first stage of the test and extends up to a limiting value of the crack tip displacement λ_{lin}.
- The second region $\lambda_{lin} < \lambda$, where $\theta \neq \varphi$ and $Cos^{-1}(\theta\text{-}\varphi) > 1$, corresponds to the nonlinear part of the displacement path. A closer look at this region shows that for a given value of λ_F, the evolution of $Cos^{-1}(\theta\text{-}\varphi)$ varies for both the MMB 50% and 75% tests.

Analyzing the early stages of the test and the λ_{lin} for both MMB 50% and 75%, it can be seen that for MMB 50%, the cohesive law behaves a truss like at a crack tip displacement magnitude $\lambda_{lin} = 0.03$–0.04 mm while for MMB 75% this phenomenon occurs for $\lambda_{lin} = 0.04$–0.05 mm, regardless of the specimen configuration.

In order to analyze the effect of the adhesive thickness and the adherend thickness on the evolution of $Cos^{-1}(\theta\text{-}\varphi)$ in detail, Fig. 12**a**

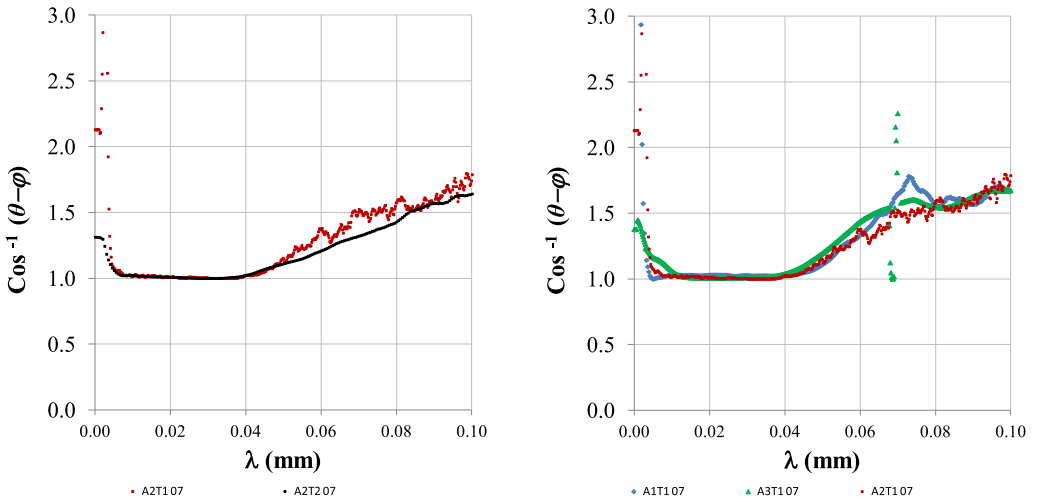

Fig. 12. Evolution of $Cos^{-1}(\theta\text{-}\varphi)$ for MMB75 a) Adhesive thickness effect b)Adhered thickness effect.

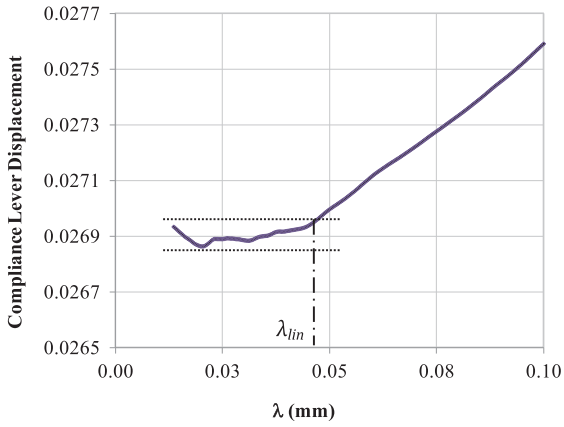

Fig. 13. Lever displacement compliance (mm/N) vs crack tip displacement magnitude for the specimen A1T1 for MMB75.

shows the evolution of $Cos^{-1}(\theta\text{-}\varphi)$ for different adhesive thicknesses corresponding to the specimens A2T1 and A2T2 for MMB75%. In Fig. 12**b** the evolution of $Cos^{-1}(\theta\text{-}\varphi)$ for different adherend thicknesses corresponding to the specimens A1T1, A2T1 and A3T1 for MMB75% is depicted. Similar results have been obtained for MMB50%.

According to Fig. 12**a and 12b**, the adhesive and adherend thickness effect on λ_{lin} is either nonexistent or small enough to fall within the experimental accuracy.

This lead to the hypothesis that the loss of linearity in the displacement path may be an inherent effect of the MMB test that takes place when the tested material system exhibits a large Fracture Process Zone or high plastic deformations at the crack tip.

In order to develop this idea, the model based on the Equivalent Crack Length approach (ECL) is considered [36,37,38].

ECL is a beam theory based method that assumes that every effect associated to the damage development is included in the equivalent crack length obtained based on the compliance variation.

According to this approach, the normal component of the displacement at the crack tip Δ_n is a cubic function of the equivalent crack advance (Δa_e) [36] while the shear component of the displacement at the crack tip Δ_t is a quadratic function [36,37].

Assuming as damage parameter the equivalent crack advance, in a first stage, when the equivalent crack advance is small Δa_e ^{3,2} $\ll\ll\Delta a_e$, both the normal and the shear component of the crack tip displacement are first order functions of Δa , thus according to the ECL, the displacement path is linear, giving rise to $Cos^{-1}(\theta\text{-}\varphi) = 1$ and a truss-like behavior.

However, as damage develops, the failure process zone increases, which according to ECL model gives rise to a large Δa_e that causes the two functions of different order Δ_n and Δ_t to vary differently, giving rise to the φ variation and accordingly to $Cos^{-1}(\theta\text{-}\varphi) > 1$.

To support the conclusion in the previous paragraph, Fig. 13 shows the lever displacement compliance with respect to the crack tip displacement magnitude for the specimen A1T1 for MMB75.

According to compliance based methods [36 37 38], the equivalent crack advance is directly related to the variation of the compliance. Fig. 13 shows that the compliance undergoes a slight variation in the early stages of the test, which implies a small equivalent crack advance, up to a crack tip displacement value matching with the aforementioned limit of the linear displacement path λ_{lin}. It can be seen that from this point onwards, the variation of the compliance increases, which implies a larger crack advance and the consequent nonlinearity of the displacement path.

Therefore, when the tested material system presents a Fracture Process Zone or plastic deformations at the crack tip that exceed a certain size associated with a Δa_e , the displacement path will lose linearity once the threshold is exceeded, regardless the final size of the FPZ that depends on the specimen configuration (eg. different adherend or adhesive thickness). Taking a look at the evolution of $Cos^{-1}(\theta\text{-}\varphi)$ in the nonlinear region, the curve shows a change of trend for a value $\lambda = \lambda_F$ which can be explained by the presence of friction. According to Figs. 10 and 11, for a mixed mode ratio of 50%, $\lambda_F = 0.06$–0.07 mm while for a mixed mode ratio of 75% this phenomenon occurs for $\lambda_F = 0.07$–0.08 mm, regardless of the specimen configuration.

In order to prove the assumption of frictional effects, the shear stress component vs. the shear displacement component curves are depicted in Fig. 14 comparing results of MMB50% and MMB 75% with the pure Mode II ENF test results [24].

All the curves in Fig. 14 show a change in the softening tendency with the emergence of a remanent stress, which can be related as mentioned above, with the presence of friction in the fractured interface or friction because of the extension of the FPZ to the midpoint loading position, which increases with increasing the mode II ratio.

The values of λ corresponding to those values of Δ_t shown at Fig. 14 at which the effects of friction arise, coincide with the λ_F defined above for all the tested configurations.

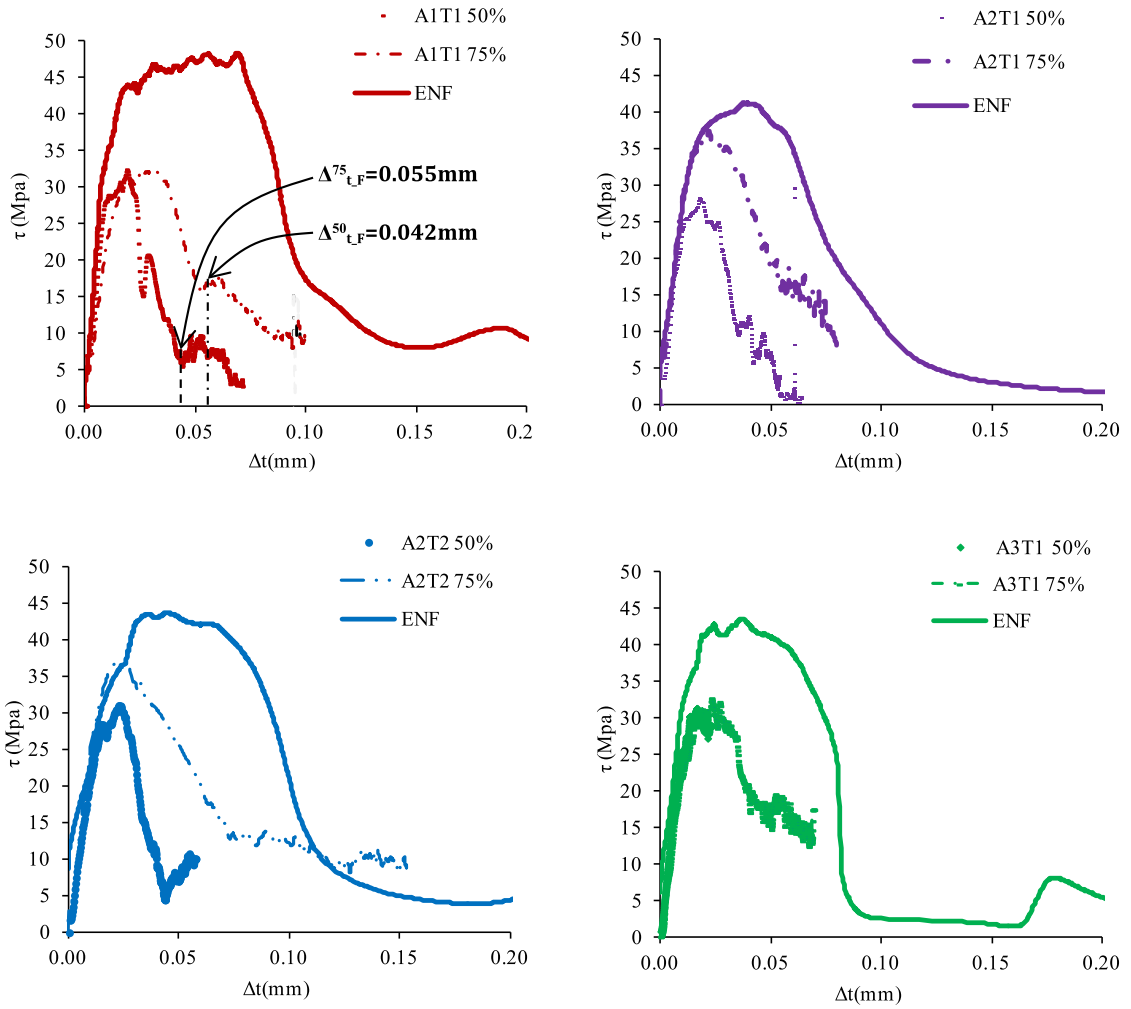

Fig. 14. Shear stress component for applied mixed-mode ratio of 75%, 50% and Pure Mode II. a) A1T1 upper left; b) A2T1 upper right; c) A2T2 bottom left y d) A3T1 bottom right.

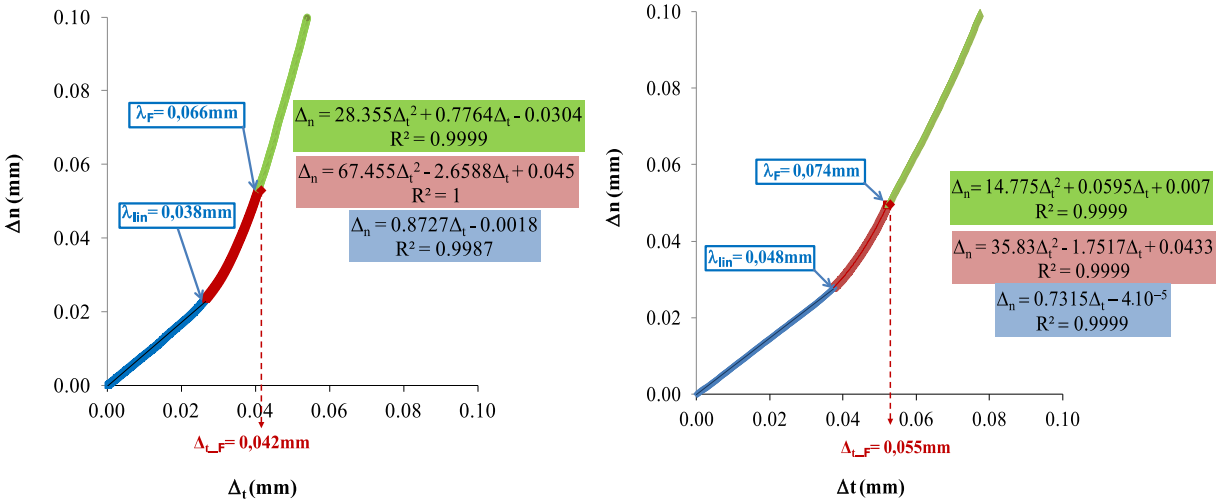

Fig. 15. Evolution of the displacement path of A1T1 for MMB50 on the left and A1T1 for MMB75 on right.

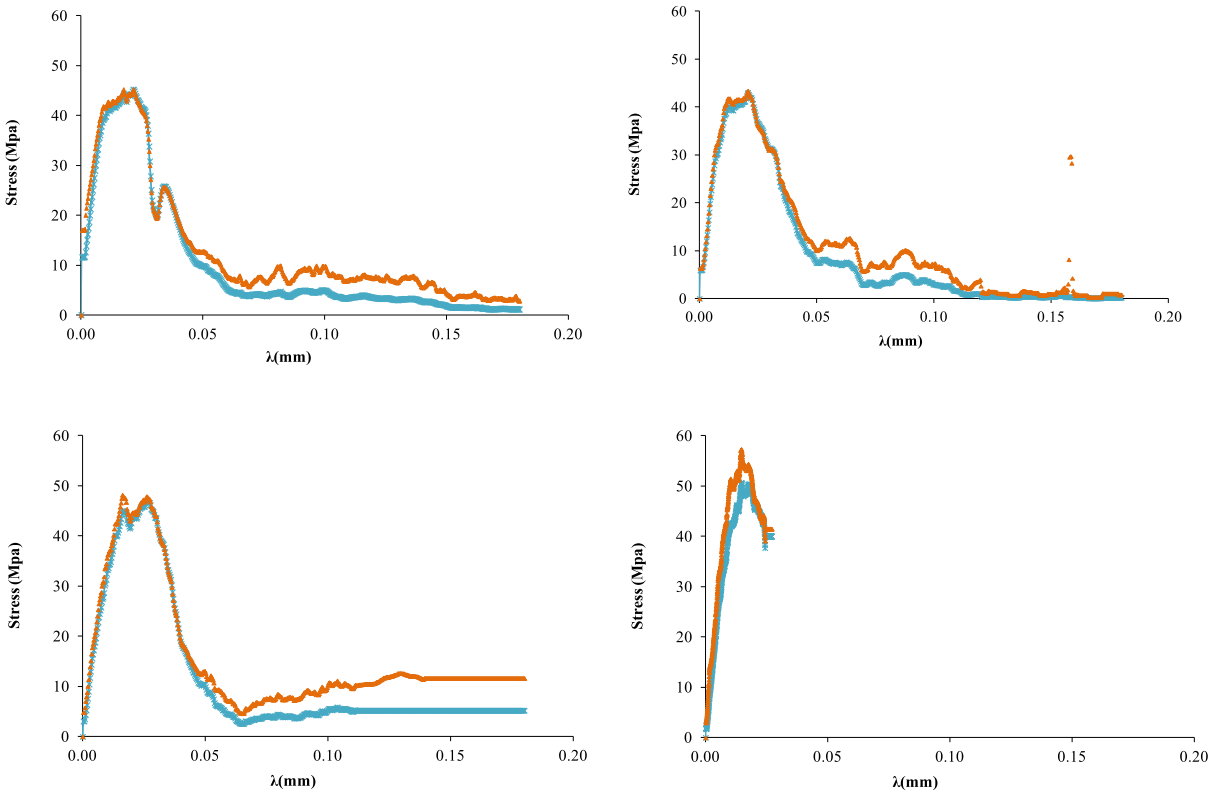

Fig. 16. Cohesive laws for applied mixed-mode ratio of 50%, results based on Eq. (7) in orange and results from Eq. (13) in blue for the following specimens: **Upper left**: A1T1; **Upper right**: A2T1; **Bottom Left**: A2T2; **Bottom Right**: A3T1. (For interpretation of the references to colour in this figure legend, the reader is referred to the web version of this article.)

In order to give confirmation evidence, the displacement paths of the specimens A1T1 MMB 50% and A1T1 MMB 75% are plotted in Fig. 15. Three regions delimited by the experimentally determined λ_{lin} y λ_F displacement values are fitted to linear and quadratic polynomial curves, respectively.

According to Fig. 14**a** the stress steady value arises at $\Delta_t = 0.042$ mm for the MMB50 and $\Delta_t = 0.055$ mm for the MMB 75 and the corresponding λ_F values are $\lambda_F = 0.066$ mm and $\lambda_F = 0.074$ mm, respectively.

On the other hand, the λ_{lin} values of the specimens A1T1 are $\lambda_{lin} = 0.038$ mm for the MMB50 and $\lambda_{lin} = 0.048$ mm for the MMB75.

The fitting equation and the corresponding correlation parameter R of each region are shown in Fig. 15. The correlation is excellent.

Finally, the cohesive laws determined by Eq. (7)and Eq. (13) for the mixed mode ratio of 50% and 75% are compared in Figs. 16 and 17, respectively.

Figs. 16 and 17 show that, as deduced theoretically, the assumption of truss-like behavior is valid at the early stages of damage, where FPZ is still small and the displacement path is linear. It is noticeable that, for both MMB 50% and MMB 75%, and for all the tested configurations, the cohesive laws determined from Eq (7) and Eq (13) are identical up to λ_{lin}. Beyond this value, as the fracture zone develops, the displacement path becomes nonlinear and the difference between the phase angles θ and φ increases. Consequently, the behavior moves away from truss-like. As regards the remaining stress associated with friction, although it does not tend to the same value in both cases, the effect appears for the same λ_F values.

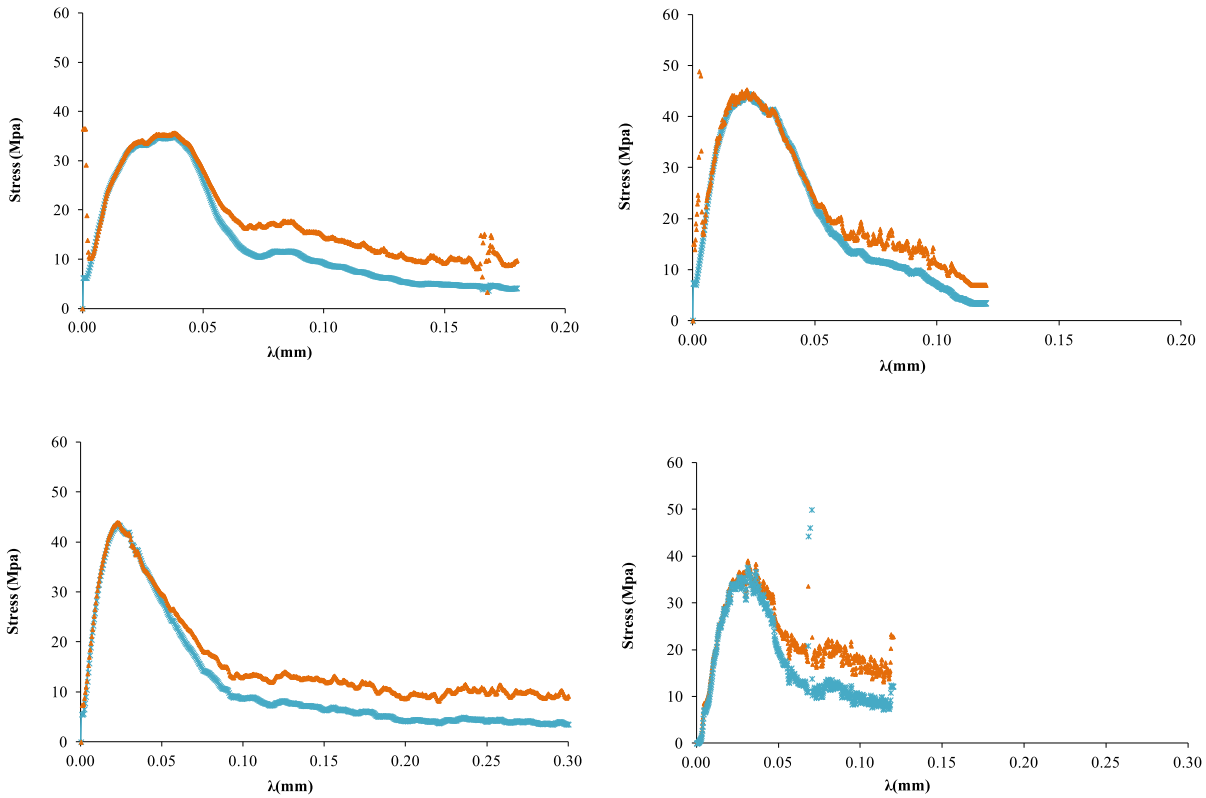

Fig. 17. Cohesive laws for applied mixed-mode ratio of 75%, results based on Eq. (7) in orange and results from Eq. (13) in blue for the following specimens: **Upper left**: A1T1; **Upper right**: A2T1; **Bottom Left**: A2T2; **Bottom Right**: A3T1. (For interpretation of the references to colour in this figure legend, the reader is referred to the web version of this article.)

6. Concluding remarks

It is theoretically set that truss like cohesive laws, where the stress vector is forced to be parallel to the displacement vector, cannot describe appropriately the fracture process when the displacement path is not linear.

An experimental proof is given to show that in a MMB test the assumption of truss like behavior is valid at the early stages of the damage, where FPZ is still small and the displacement path is linear. Beyond this value, as the fracture zone develops, the displacement path becomes nonlinear and the difference between the phase angles θ and φ increases, consequently the behavior moves away from truss-like.

The main implications are twofold: the first one is that truss-type cohesive laws, although advantageous due to their simple-to-apply formulation, can lead to differences in the predicted overall maximum load even under Linear Elastic Fracture Mechanics conditions, due to the non-linearity of the displacement path.

The second one is related to the experimental determination of the mixed mode cohesive law. It is concluded that if the displacement path becomes nonlinear, the difference between the phase angles of the stress vector and the displacement differential vector must be taken into account, so that the cohesive stress will no longer be a function only of the magnitude of the displacement.

CRediT authorship contribution statement

A. Arrese: Conceptualization, Methodology, Investigation, Writing - original draft. **F. Mujika:** Methodology, Writing - review & editing. **J. Renart:** Methodology, Writing - review & editing. **C. Sarrado:** Methodology, Writing - review & editing.

Declaration of Competing Interest

The authors declare that they have no known competing financial interests or personal relationships that could have appeared to influence the work reported in this paper.

Data availability

No data was used for the research described in the article.

Acknowledgment

Financial support of the University of the Basque Country (UPV/EHU) in the Research Group GIU 20/060 “Mechanics of Materials” is acknowledged. The authors would like to acknowledge the support of the Spanish Government though the Ministerio de Economia y Competitividad under the contract RTI2018-099373-B-I00. Open access funding provided by University of Basque Country.

References

[1] Dugdale DS. Yielding of steel sheets containing slits. J Mech Phys Solids 1960;8:100–4. https://doi.org/10.1016/0022-5096(60)90013-2.
[2] Barenblatt GI. The mathematical theory of equilibrium cracks in brittle fracture. Adv Appl Mech 1962;77:55–129. https://doi.org/10.1016/S0065-2156(08)70121-2.
[3] Park K, Paulino G. Cohesive zone models: a critical review of traction separation relationships across fracture surfaces. Appl Mech Rev 2011;64(6). https://doi.org/10.1115/1.4023110.
[4] Needleman A. A continuum model for void nucleation by inclusion debonding. J Appl Mech 1987;54:525–31. https://doi.org/10.1115/1.3173064.
[5] Tvergaard V, Hutchinson JW. The relation between crack growth resistance and fracture process parameters in elasticplastic solids. J Mech Phys Solids 1992;40:1377–97. https://doi.org/10.1016/0022-5096(92)90020-3.
[6] Yang QD, Thouless MD, Ward SM. Numerical simulations of adhesively-bonded beams failing with extensive plastic deformation. J Mech Phys Solids 1999;47(6):1337–53. https://doi.org/10.1016/S0022-5096(98)00101-X.
[7] Jacobsen TK, Sørensen BF. Mode I intra-laminar crack growth in composites modelling of R-curves from measured bridging laws. Compos Part A - Appl S 2001;32:1–11. https://doi.org/10.1016/S1359-835X(00)00139-1.
[8] Zhang ZY, Paulino GH. Cohesive zone modeling of dynamic failure in homogeneous and functionally graded materials. Int. J. Plast. 2005;21:1195–254. https://doi.org/10.1016/j.ijplas.2004.06.009.
[9] Needleman A. An analysis of tensile decohesion along an interface. J Mech Phys Solids 1990;38:289–324. https://doi.org/10.1016/0022-5096(90)90001-K.
[10] Xu XP, Needleman A. Void nucleation by inclusion debonding in a crystal matrix. Modelling Simulation Mater Sci Eng 1993;1:111–32. https://doi.org/10.1088/0965-0393/1/2/001.
[11] Tvergaard V, Hutchinson JW. The influence of plasticity on mixed mode interface toughness. J Mech Phys Solids 1993;41(6):1119–35. https://doi.org/10.1016/0022-5096(93)90057-M.
[12] Camacho GT, Ortiz M. Computational modelling of impact damage in brittle materials. Int J Solids Struct 1996;33(20–22):2899–938. https://doi.org/10.1016/0020-7683(95)00255-3.
[13] Ortiz M, Pandolfi A. Finite-deformation irreversible cohesive elements for three-dimensional crack-propagation analysis. Int J Numer Meth Eng 1999;44:1267–82. https://doi.org/10.1002/(SICI)1097-0207(19990330)44:93.3.CO;2-Z.
[14] Camanho PP, Dávila CG, de Moura MF. Numerical simulation of mixed-mode progressive delamination in composite materials. J Compos Mater 2003;37:1415–38. https://doi.org/10.1177/0021998303034505.
[15] Planas J, Sanz B, Sancho JM. Vectorial stress-separation laws for cohesive cracking: in concrete and other quasibrittle materials. Int J Fract 2020;223:77–92. https://doi.org/10.1007/s10704-019-00410-9.
[16] Goutianos S, Sorensen BF. Path dependence of truss-like mixed cohesive laws. Eng Fract Mech 2012;91:117–32. https://doi.org/10.1016/j.engfracmech.2012.02.011.
[17] Goutianos S, Sørensen BF, Thouless MD. Mixed-mode cohesive laws and the use of linear-elastic fracture mechanics. Eng Fract Mech 2021;252:107792. https://doi.org/10.1016/j.engfracmech.2021.107792.

[18] Sørensen BF. Cohesive law and notch sensitivity of adhesive joints. Acta Mater 2002;50(5):1053–61. https://doi.org/10.1016/S1359-6454(01)00404-9.
[19] Sørensen BF, Gamstedt EK, Ostergaard RC, Goutianos S. Micromechanical model of cross-over fibre bridging – prediction of mixed mode bridging laws. Mech Mater 2008;40(4–5):220–34. https://doi.org/10.1016/j.mechmat.2007.07.007.
[20] Sørensen BF, Goutianos S, Jacobsen TK. Strength scaling of adhesive joints in polymer-matrix composites. Int J Solids Struct 2009;46(3–4):741–61. https://doi.org/10.1016/j.ijsolstr.2008.09.024.
[21] Suo Z, Bao G, Fan B. Delamination R-curve phenomena due to damage. J Mech Phys Solids. 1992;40:1–16. https://doi.org/10.1016/0022-5096(92)90198-B.
[22] Sørensen BF, Kirkegaard P. Determination of mixed mode cohesive laws. Eng Fract Mech 2006;73:2642–61. https://doi.org/10.1016/j.engfracmech.2006.04.006.
[23] Hogberg JL, Sørensen BF, Stigh U. Constitutive behavior of mixed mode loaded adhesive layer. 2007;44:8335–54. https://doi.org/10.1016/j.ijsolstr.2007.06.014.
[24] Sarrado C, Turon A, Costa J, Renart J. An experimental analysis of the fracture behavior of composite bonded joints in terms of cohesive laws. Compos Part A 2016;90:234–42. https://doi.org/10.1016/j.compositesa.2016.07.004.
[25] Oliveira J, Xavier J, Pereira F, Morais J, Moura M. Direct Evaluation of Mixed Mode I+II Cohesive Laws of Wood by Coupling MMB Test with DIC. Materials 2021;14:374. https://doi.org/10.3390/ma14020374.
[26] Rice JR. A path independent integral and the approximate analysis of strain concentration by notches and cracks. J Appl Mech 1968;35:379–86. https://doi.org/10.1115/1.3601206.
[27] Loh L, Marzi S. A novel experimental methodology to identify fracture envelopes and cohesive laws in mixed-mode i+iii. Eng Fract Mech 2019;214:304–19. https://doi.org/10.1016/J.ENGFRACMECH.2019.03.011.
[28] Ji G, Ouyang Z, Li G. On the interfacial constitutive laws of mixed mode fracture with various adhesive thicknesses. Mech Mater 2012;47:24–32. https://doi.org/10.1016/j.mechmat.2012.01.002.
[29] Liu W, Chen P. Determination of the bridging law for mixed-mode I/II delamination without measuring the crack length and crack relative displacements. Theor Appl Fract Mech 2020;109:102750. https://doi.org/10.1016/J.ENGFRACMECH.2020.106867.
[30] ASTM D6671/D6671M-06. Standard test method for mixed mode I-mode II interlaminar fracture toughness of unidirectional fiber reinforced polymer matrix composites. American Society for Testing and Materials; 2006.
[31] Sorensen BF. Cohesive law and notch sensitivity of adhesive joints. Acta Mater 2002;70:1053–61. https://doi.org/10.1016/S1359-6454(01)00404-9.
[32] Sarrado C, Turon A, Renart J, Costa J. An experimental data reduction method for the Mixed Mode Bending test based on the J-integral approach. Compos Sci Technol 2015;117:85–91. https://doi.org/10.1016/j.compscitech.2015.05.021.
[33] Hogberg JL, Sørensen BF, Stigh U. Constitutive behaviour of mixed mode loaded adhesive layer. Int J Solids Struct 2007;44(25–26):8335–54. https://doi.org/10.1016/j.ijsolstr.2007.06.014.
[34] Turon A, Camanho PP, Costa J, Renart J. Accurate simulation of delamination growth under mixed-mode loading using cohesive elements: definition of interlaminar strengths and elastic stiffness. Compos Struct 2010;92(8):1857–64. https://doi.org/10.1016/j.compstruct.2017.10.017.
[35] Sarrado C, Turon A, Renart J, Urresti I. Assessment of energy dissipation during mixed-mode delamination growth using cohesive zone models. Compos Part A - Appl Sci Manuf 2012;43(11):2128–36. https://doi.org/10.1016/J.COMPOSITESA.2012.07.009.
[36] Arrese A, Boyano A, de Gracia J, Mujika F. A novel procedure to determine the cohesive law in DCB tests. Compos Sci. Technol 2017;152:76–84. https://doi.org/10.1016/j.compscitech.2017.09.012.
[37] Arrese A, Insausti N, Mujika F, Perez-Galmés M, Renart J. A novel procedure to determine the cohesive law in ENF tests. Compos Sci. Technol 2019;170:42–50. https://doi.org/10.1016/j.compscitech.2018.11.031.
[38] Arrese A, Adarraga I, Insausti N, Renart J, Sarrado C. Mode II cohesive law extrapolation procedure of composite bonded joints. Eng. Fract. Mech. 2021;244:107563. https://doi.org/10.1016/j.engfracmech.2021.107563.